A comprehensive FE model for slender HSC columns under biaxial eccentric loads

Tiejiong Lou[1,2], Sergio M. R. Lopes[3], Adelino V. Lopes[3] and Wei Sun[*2]

[1]*Hubei Key Laboratory of Roadway Bridge & Structure Engineering, Wuhan University of Technology, 430070 Wuhan, China*

[2]*Faculty of Engineering and Physical Sciences, University of Southampton, SO17 1BJ Southampton, United Kingdom*

[3]*Department of Civil Engineering, University of Coimbra, 3030-788 Coimbra, Portugal*

(Received , Revised , Accepted)

Abstract. A finite element (FE) model for analyzing slender reinforced high-strength concrete (HSC) columns under biaxial eccentric loading is formulated in terms of the Euler-Bernoulli theory. The cross section of columns is divided into discrete concrete and reinforcing steel fibers so as to account for varied material properties over the section. The interaction between axial and bending fields is introduced in the FE formulation so as to take the large-displacement or P-delta effects into consideration. The proposed model aims to be simple, user-friendly, and capable of simulating the full-range inelastic behavior of reinforced HSC slender columns. The nonlinear model is calibrated against the experimental data for slender column specimens available in the technical literature. By using the proposed model, a numerical study is carried out on pin-ended slender HSC square columns under axial compression and biaxial bending, with investigation variables including the load eccentricity and eccentricity angle. The calibrated model is expected to provide a valuable tool for more efficiently designing HSC columns.

Keywords: Slender columns; High-strength concrete; Finite element method; Biaxial bending

1. Introduction

Nowadays, as the global population has been increasing considerably, the demands for high-rise buildings become more and more urgent. This suggests a great potential for using

* Corresponding author, Ph.D., Marie Curie Fellow, E-mail: Wei.Sun@soton.ac.uk

high-strength concrete (HSC) to achieve light-weight concrete elements by reducing the cross-section dimension (Jumaa and Yousif 2019). Moreover, a reduced cross section also suggests a less demand for concrete material, an easier construction because of the light-weight merit, and a reduced consumption of embodied energy achieving one step forward towards low impact buildings. On the other hand, however, a reduced cross section further deteriorates the impact of slenderness on HSC columns, i.e. P-delta effects (Diniz and Frangopol 2003, Hung and Hu 2018). These effects have been demonstrated to be crucial to both the instantaneous and time-dependent response of a slender column (Lou *et al*. 2015a).

Despite the brittleness of HSC, HSC members with appropriate reinforcement were shown to exhibit favorable ductile behavior (Bouzid and Kassoul 2016, 2018, Lee 2013, Lou *et al*. 2015b, 2017, Ma *et al*. 2016, Teixeira and Bernardo 2018). Over past years, many works have been reported on the analysis and design of HSC short columns (Bai and Au 2013, Campione *et al*. 2012, Diniz and Frangopol 1998, Ho *et al*. 2010, Saatcioglu and Razvi 1998). In these columns, the P-delta effects were negligible and the inelastic behavior was identified by means of the material nonlinear analysis of a single cross-section. Some research has been conducted to simulate the behavior of slender HSC columns, mostly under the uniaxial loading condition, by performing geometric and material nonlinear analysis. Diniz and Frangopol (1997) outlined a simplified analytical approach to analyze the strength as well as interaction diagram of axial force and bending moment of uniaxially loaded slender HSC columns. Kim and Yang (1995) proposed a finite element (FE) method to predict the buckling behavior of slender HSC columns subjected to axial compression and uniaxial bending. Claeson and Gylltoft (1998) conducted a parametric study using the software ABAQUS on the performance of uniaxially loaded slender HSC square columns, focusing on the effects of concrete strength, slenderness and load eccentricity. Nevertheless, few efforts have so far been made to analyze the performance of HSC slender columns under biaxial eccentric loads. Pallarés *et al*. (2009) performed a numerical investigation, using a nonlinear model validated against their own tests (2008), on the behavior of slender HSC columns under axial compression and biaxial bending. The emphasis of their study was placed on the effect of the weak axis on the member performance. Bouchaboub and Samai (2013) described a nonlinear model for biaxially loaded HSC slender columns. Their model was developed based on the moment-curvature-thrust relationships and by applying the finite difference method. However, the overall performance of slender HSC columns was not numerically investigated in their work.

The FE method offers a powerful technique to simulate the real structural performance of different types of concrete members. Although commercial FE software is capable of analyzing the inelastic behavior of HSC columns (Teng *et al*. 2015), there are still demands for self-developed FE models to further aid the design of column preventing a vast investment on the software license. However, the studies with an emphasis on developing such FE models considering both axial and biaxial impacts are currently few in number. This paper presents the development of a FE model

for slender reinforced HSC columns subjected to axial compression and biaxial bending. The method is formulated based on the spatial Euler-Bernoulli theory, taking into account geometric and material nonlinearities. The model predictions are compared with the experimental results available in the literature. A numerical investigation is performed by using the proposed model to increase the depth of understanding of the inelastic response of slender HSC columns under eccentric end axial loads causing biaxial bending.

2. Material models

The stress-strain relationship for unconfined concrete in compression recommended in Eurocode 2 (CEN 2004) has been proved to be suitable for nonlinear analysis of both NSC and HSC members. The stress-strain equation is expressed by

$$\frac{\sigma_c}{f_{cm}} = \frac{k\eta - \eta^2}{1 + (k-2)\eta} \tag{1}$$

where $\eta = \varepsilon_c / \varepsilon_{c0}$; σ_c and ε_c are the concrete stress and strain, respectively; f_{cm} is the mean compressive strength (in MPa), and $f_{cm} = f_{ck} + 8$; f_{ck} is the characteristic cylinder compressive strength (in MPa); $k = 1.05 E_c \varepsilon_{c0} / f_{cm}$; $\varepsilon_{c0}(‰) = 0.7 f_{cm}^{0.31} < 2.8$; E_c is the modulus of elasticity of concrete (in GPa), and $E_c = 22(f_{cm}/10)^{0.3}$. Eq. (1) is valid for $\varepsilon_c \le \varepsilon_u$, where ε_u is the ultimate compressive strain. $\varepsilon_u(‰) = 3.5$ for NSC; and $\varepsilon_u(‰) = 2.8 + 27[(98 - f_{cm})/100]^4$ for HSC.

An elastic and linear tension-stiffening law is adopted for concrete in tension. The tensile strength f_t is determined by

$$f_t = 0.3 f_{ck}^{2/3} \quad \text{for NSC} \tag{2a}$$

$$f_t = 2.12 \ln(1 + f_{cm}/10) \quad \text{for HSC} \tag{2b}$$

The reinforcing steel is assumed to be elastic and perfectly plastic, i.e.

At elastic range, $$\sigma_s = E_s \varepsilon_s \tag{3a}$$

After yielding, $$\sigma_s = f_y \tag{3b}$$

where σ_s and ε_s are the steel stress and strain, respectively; E_s and f_y are the steel modulus of elasticity and yield strength, respectively.

3. FE method

Consider a two-node space beam element in the local coordinate system (x, y, z), as shown in Fig. 1(a). Each node has five degrees of freedom, namely, x-displacement u, y-displacement v, z-displacement w, rotations about y-axis θ_y and z-axis θ_z. The element nodal displacements may be written as

$$\boldsymbol{r}^e = \{u_1, v_1, w_1, \theta_{y1}, \theta_{z1}, u_2, v_2, w_2, \theta_{y2}, \theta_{z2}\}^T \tag{4}$$

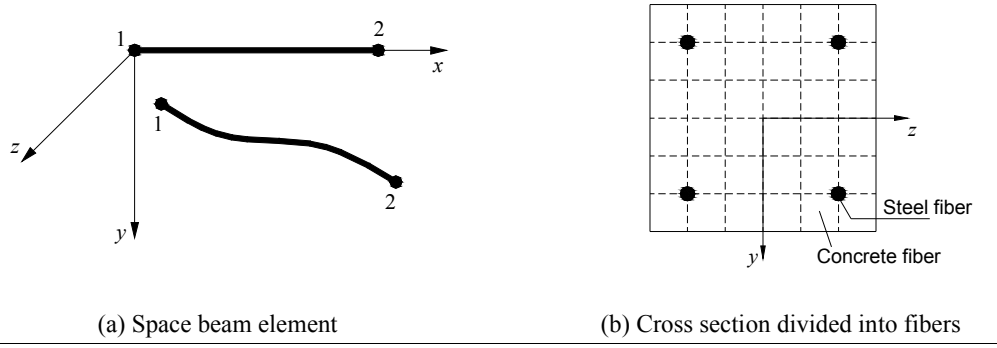

(a) Space beam element (b) Cross section divided into fibers

Fig. 1 Computational model

Assuming that u is a linear function whereas v and w are both a cubic polynomial of x, these displacements are then related to the element nodal displacements by

$$u = N_1 u_1^e + N_6 u_2^e \tag{5a}$$

$$v = N_2 v_1^e + N_5 \theta_{z1}^e + N_7 v_2^e + N_{10} \theta_{z2}^e \tag{5b}$$

$$w = N_3 w_1^e + N_4 \theta_{y1}^e + N_8 w_2^e + N_9 \theta_{y2}^e \tag{5c}$$

in which $N_1 = 1-\xi$; $N_2 = 1-3\xi^2+2\xi^3$; $N_3 = N_2$; $N_4 = l(\xi-2\xi^2+\xi^3)$; $N_5 = N_4$; $N_6 = \xi$; $N_7 = 3\xi^2-2\xi^3$; $N_8 = N_7$; $N_9 = l(-\xi^2+\xi^3)$; $N_{10} = N_9$; $\xi = x/l$ where l is the element length.

At any point on an element, the axial strain ε_O can be expressed by

$$\varepsilon_O = u' + (v')^2/2 + (w')^2/2 \tag{6}$$

in which a superimposed prime represents differentiation with respect to x. The second and third terms of the right-hand side of the preceding equation represent the large displacement effects. On the other hand, by assuming negligible shear deformation, the curvatures about y axis ϕ_y and z

axis ϕ_z can be expressed as

$$\phi_y = -w'' \; ; \;\; \phi_z = -v'' \tag{7}$$

Combining Eqs. (4) through (7), the axial strain and biaxial curvatures are related to the element nodal displacements, in a matrix form, by

$$\boldsymbol{E} = \left(\boldsymbol{B}_l + \boldsymbol{B}_n / 2 \right) \boldsymbol{r}^e \tag{8}$$

where

$$\boldsymbol{E} = \left\{ \varepsilon_O \quad \phi_y \quad \phi_z \right\}^T \tag{9}$$

$$\boldsymbol{B}_l = \begin{bmatrix} N_1' & 0 & 0 & 0 & 0 & N_6' & 0 & 0 & 0 & 0 \\ 0 & -N_2'' & 0 & 0 & -N_5'' & 0 & -N_7'' & 0 & 0 & -N_{10}'' \\ 0 & 0 & -N_3'' & -N_4'' & 0 & 0 & 0 & -N_8'' & -N_9'' & 0 \end{bmatrix} \tag{10a}$$

$$\boldsymbol{B}_n = \begin{bmatrix} 1 & 0 & 0 \end{bmatrix}^T \boldsymbol{r}^{eT} \left(\boldsymbol{J}_1^T \boldsymbol{J}_1 + \boldsymbol{J}_2^T \boldsymbol{J}_2 \right) \tag{10b}$$

$$\boldsymbol{J}_1 = \begin{bmatrix} 0 & N_2' & 0 & 0 & N_5' & 0 & N_7' & 0 & 0 & N_{10}' \end{bmatrix} \tag{11a}$$

$$\boldsymbol{J}_2 = \begin{bmatrix} 0 & 0 & N_3' & N_4' & 0 & 0 & 0 & N_8' & N_9' & 0 \end{bmatrix} \tag{11b}$$

It is noted that $\boldsymbol{B}_l$ is a linear matrix whereas $\boldsymbol{B}_n$ is a nonlinear matrix. Hence the variational form of Eq. (8) can be written as

$$\delta \boldsymbol{E} = \boldsymbol{B}_l \delta \boldsymbol{r}^e + \frac{1}{2} \begin{bmatrix} 1 & 0 & 0 \end{bmatrix}^T \boldsymbol{r}^{eT} \left(\boldsymbol{J}_1^T \boldsymbol{J}_1 + \boldsymbol{J}_2^T \boldsymbol{J}_2 \right) \delta \boldsymbol{r}^e + \frac{1}{2} \begin{bmatrix} 1 & 0 & 0 \end{bmatrix}^T \delta \boldsymbol{r}^{eT} \left(\boldsymbol{J}_1^T \boldsymbol{J}_1 + \boldsymbol{J}_2^T \boldsymbol{J}_2 \right) \boldsymbol{r}^e$$

$$= \boldsymbol{B}_l \delta \boldsymbol{r}^e + \begin{bmatrix} 1 & 0 & 0 \end{bmatrix}^T \boldsymbol{r}^{eT} \left(\boldsymbol{J}_1^T \boldsymbol{J}_1 + \boldsymbol{J}_2^T \boldsymbol{J}_2 \right) \delta \boldsymbol{r}^e$$

$$= \left(\boldsymbol{B}_l + \boldsymbol{B}_n \right) \delta \boldsymbol{r}^e \tag{12}$$

To take into account varied material properties across a cross section that is subjected to axial force and biaxial bending, the cross section is divided into concrete and reinforcing steel fibers as shown in Fig. 1(b). The strain in each fiber is assumed to be uniformly distributed. The equilibrium of axial force and biaxial bending moments can then be expressed as follows:

$$P = \sum_i \sigma_{ci} A_{ci} + \sum_j \sigma_{sj} A_{sj} \tag{13a}$$

$$M_y = \sum_i \sigma_{ci} A_{ci} z_{ci} + \sum_j \sigma_{sj} A_{sj} z_{sj} \tag{13b}$$

$$M_z = \sum_i \sigma_{ci} A_{ci} y_{ci} + \sum_j \sigma_{sj} A_{sj} y_{sj} \tag{13c}$$

where P is the axial force; M_y is the bending moment about the y-axis and M_z is the bending moment about the z-axis; The symbol A represents the area and σ represents the stress; The subscripts ci and sj represent the ith concrete fiber and jth steel fiber, respectively. The tangential force-strain equations are

$$dP = \sum_i E_{tci} A_{ci} d\varepsilon_{ci} + \sum_j E_{tsj} A_{sj} d\varepsilon_{sj} \tag{14a}$$

$$dM_y = \sum_i E_{tci} A_{ci} z_{ci} d\varepsilon_{ci} + \sum_j E_{tsj} A_{sj} z_{sj} d\varepsilon_{sj} \tag{14b}$$

$$dM_z = \sum_i E_{tci} A_{ci} y_{ci} d\varepsilon_{ci} + \sum_j E_{tsj} A_{sj} y_{sj} d\varepsilon_{sj} \tag{14c}$$

in which E_t represents the tangential modulus of materials and ε represents the strain.

Based on the plane section assumption, the axial strain ε at any fiber of a cross section is given by

$$\varepsilon = \varepsilon_O + z\phi_y + y\phi_z \tag{15}$$

Differentiating the preceding equation with respect to ε_O, ϕ_y and ϕ_z gives

$$d\varepsilon = d\varepsilon_O + z d\phi_y + y d\phi_z \tag{16}$$

Substituting Eq. (16) into Eq. (14) yields section tangential stiffness equations:

$$d\boldsymbol{S} = \boldsymbol{Q} d\boldsymbol{E} \tag{17}$$

$$\boldsymbol{S} = \begin{Bmatrix} P & M_y & M_z \end{Bmatrix}^T \tag{18}$$

$$\boldsymbol{Q} = \begin{bmatrix} q_{11} & q_{12} & q_{13} \\ q_{21} & q_{22} & q_{23} \\ q_{31} & q_{32} & q_{33} \end{bmatrix} \tag{19}$$

$$q_{11} = \sum_i E_{tci} A_{ci} + \sum_j E_{tsj} A_{sj} \tag{20a}$$

$$q_{12} = q_{21} = \sum_i E_{tci} A_{ci} z_{ci} + \sum_j E_{tsj} A_{sj} z_{sj} \tag{20b}$$

$$q_{13} = q_{31} = \sum_i E_{tci} A_{ci} y_{ci} + \sum_j E_{tsj} A_{sj} y_{sj} \tag{20c}$$

$$q_{22} = \sum_i E_{tci} A_{ci} z_{ci}^2 + \sum_j E_{tsj} A_{sj} z_{sj}^2 \tag{20d}$$

$$q_{23} = q_{32} = \sum_i E_{tci} A_{ci} y_{ci} z_{ci} + \sum_j E_{tsj} A_{sj} y_{sj} z_{sj} \tag{20e}$$

$$q_{33} = \sum_i E_{tci} A_{ci} y_{ci}^2 + \sum_j E_{tsj} A_{sj} y_{sj}^2 \tag{20f}$$

Based on the principle of virtual work, the equilibrium equations for a beam element are expressed by: $\delta \boldsymbol{r}^{eT} \boldsymbol{R}^e = \int_l \delta \boldsymbol{E}^T \boldsymbol{S} dx$, where $\boldsymbol{R}^e$ is the element equivalent nodal loads. Substituting Eq. (12) into the preceding virtual work equations yields

$$\boldsymbol{R}^e = \int_l (\boldsymbol{B}_l^T + \boldsymbol{B}_n^T) \boldsymbol{S} dx \tag{21}$$

The differential form of Eq. (21) with respect to $\boldsymbol{r}^e$ can be written as follows:

$$d\boldsymbol{R}^e = \int_l (\boldsymbol{B}_l^T + \boldsymbol{B}_n^T) d\boldsymbol{S} dx + \int_l d\boldsymbol{B}_n^T \boldsymbol{S} dx \tag{22}$$

Substituting Eqs. (17) and (12) sequentially into Eq. (22), and rearranging the resulting equation, the element tangential stiffness equations can be obtained:

$$d\boldsymbol{R}^e = (\boldsymbol{K}_1^e + \boldsymbol{K}_2^e + \boldsymbol{K}_3^e) d\boldsymbol{r}^e \tag{23}$$

$$\boldsymbol{K}_1^e = \int_l \boldsymbol{B}_l^T \boldsymbol{Q} \boldsymbol{B}_l dx \tag{24a}$$

$$\boldsymbol{K}_2^e = \int_l \boldsymbol{B}_l^T \boldsymbol{Q} \boldsymbol{B}_n dx + \int_l \boldsymbol{B}_n^T \boldsymbol{Q} \boldsymbol{B}_l dx + \int_l \boldsymbol{B}_n^T \boldsymbol{Q} \boldsymbol{B}_n dx \tag{24b}$$

$$\boldsymbol{K}_3^e = \int_l P(\boldsymbol{J}_1^T \boldsymbol{J}_1 + \boldsymbol{J}_2^T \boldsymbol{J}_2) dx \tag{24c}$$

where $\boldsymbol{K}_1^e$ is the small displacement stiffness matrix; $\boldsymbol{K}_2^e$ is the coupling stiffness matrix; and $\boldsymbol{K}_3^e$ is the geometric stiffness matrix.

After assembling the structure equilibrium equations in the global coordinate system, a load or displacement control incremental method combined with the Newton-Raphson iterative algorithm is applied for the numerical solution. The iterative procedure for each increment is summarized as follows:

- Form or update element tangential stiffness matrices, and assemble them into the structure tangential stiffness matrix.
- Solve equilibrium equations for displacement increments.
- Add displacement increments to the previous total to obtain the current nodal displacements.
- In the local coordinate system, compute the axial strain ε_O and biaxial curvatures ϕ_y, ϕ_z using Eq. (8).
- Calculate the strain ε in each concrete or steel fiber using Eq. (15), and substitute it into the stress-strain relationship to get the material stress σ. Compute the axial force *P* and biaxial moments M_y, M_z using Eq. (13).

- Compute the element end forces using the right-hand side of Eq. (21) and then assemble them into the internal resisting forces.
- Compute the out-of-balance loads by subtracting the internal resisting forces from the current nodal loads.
- Repeat the above steps until the out-of-balance loads are within the permissible tolerance.

A computer program implementing the present numerical procedure has been developed. The program needs the input of material properties, column length, cross-sectional dimensions, boundary conditions and load pattern. At any particular load level, the output includes nodal displacement and rotation, moment and curvature, stress and strain in concrete and reinforcing steel. The program is able to simulate the behavior of slender HSC columns under biaxial eccentric loads throughout the elastic, inelastic and ultimate limit states. In the following sections, the proposed analysis is used to reproduce the experimental results of slender column specimens available in the technical literature and to perform a numerical investigation into the inelastic behavior of HSC slender columns under biaxial bending.

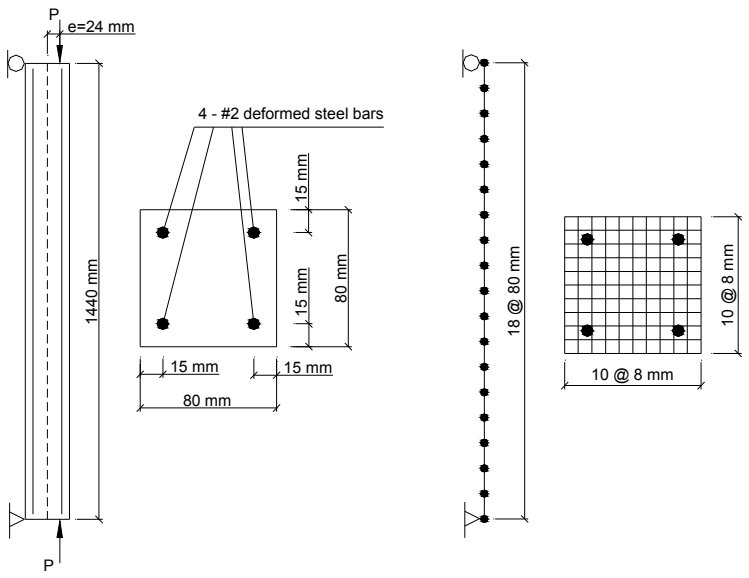

(a) Column details (b) FE model

Fig. 2 Test columns and FE model

4. Comparisons with experimental data

Kim and Yang (1995) tested a series of NSC and HSC slender square columns up to failure.

The test variables included the span length, concrete strength and longitudinal steel ratio. The structure details and cross section of the test columns selected for the present analysis are shown in Fig. 2(a). These columns had a span length of 1440 mm, reinforcing steel ratio of 1.98% and three different levels of concrete strength f_{cm}, namely, 25.5 (Columns 60L2-1 and 60L2-2), 63.5 (Columns 60M2-1 and 60M2-2) and 86.2 MPa (Columns 60H2-1 and 60H2-2). The yield strength and elastic modulus of reinforcing steel were 387 MPa and 200 GPa, respectively. The load eccentricity was 24 mm.

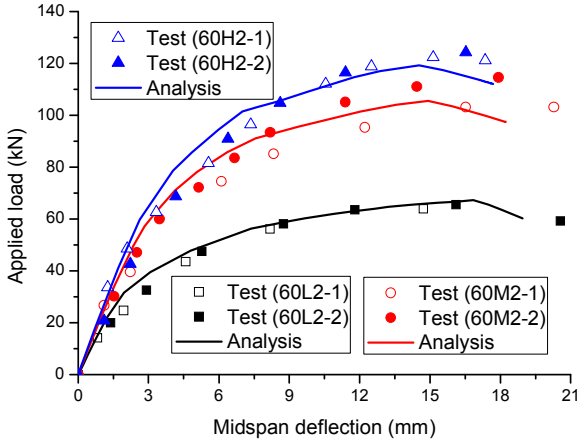

Fig. 3 Comparison of predicted load-deflection curves with experimental results for the test columns

Table 1 Comparison with experimental data for the test columns

Column	Concrete strength (MPa)	Maximum load			Deflection at maximum load		
		Test (kN)	Analysis (kN)	Error (%)	Test (MPa)	Analysis (MPa)	Error (%)
60L2-1	25.5	63.7	67.2	5.49	14.88	16.84	13.17
60L2-2		65.7	67.2	2.28	16.20	16.84	3.95
60M2-1	63.5	102.8	105.6	2.72	20.32	14.92	-26.57
60M2-2		113.5	105.6	-6.96	18.08	14.92	-17.48
60H2-1	86.2	122.1	119.2	-2.38	15.40	14.55	-5.52
60H2-2		123.7	119.2	-3.64	16.72	14.55	-12.98

The column is divided into 18 beam elements, and the cross section is divided into 10 × 10 concrete fibers and 4 steel fibers, as shown in Fig. 2(b). The predicted load versus midspan lateral

deflection curves are compared with the experimentally obtained data in Fig. 3. It is generally observed that the proposed analysis reproduces the entire load-deflection response characteristics for the test columns with good accuracy. A comparison of the test and calculated values of the maximum load and corresponding deflection is given in Table 1. The correlation coefficient between the values of the maximum load is 0.992, and the average discrepancy is -0.41%, with a standard deviation of 4.67%. The correlation coefficient between the values of the lateral deflection at the maximum load is -0.429, and the average discrepancy is -7.57%, with a standard deviation of 14.53%. The proposed model appears to overestimate the maximum load for the NSC columns while underestimate the maximum load for the HSC columns. This may be attributed to the difference in the actual and reported concrete strengths for the column specimens.

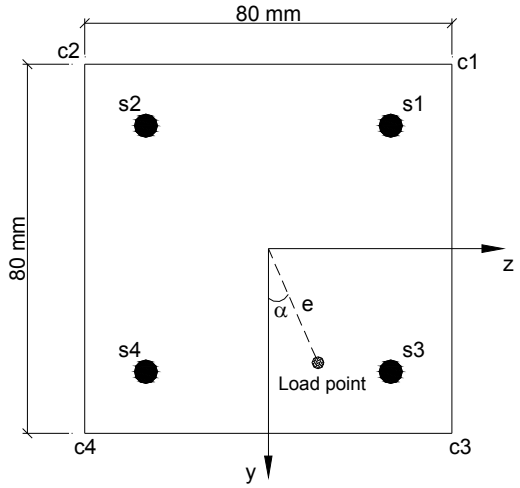

Fig. 4 Cross section of columns used for numerical investigation

5. Numerical application

The HSC column (i.e., Column 60H2-1 or 60H2-2) tested by Kim and Yang (1995) is selected herein as a reference column for the investigation. A numerical study is carried out to evaluate the inelastic behavior of biaxially loaded slender HSC columns with investigation variables including the load eccentricity e and eccentricity angle α (see Fig. 4). Two eccentricity levels are used, namely, e = 24 and 48 mm; and three different eccentricity angles are considered, namely, α = 0°, 30° and 45°. The four steel bars are designated as s1-s4, and the concrete fibers at four vertices of

the cross section are represented by c1-c4, as shown in Fig. 4.

5.1 Moment-curvature behavior

Fig. 5 shows the moment-curvature curves at midspan for the HSC columns with different load eccentricities and eccentricity angles. Both the biaxial moment-curvature diagrams with respect to y and z-axes (i.e. M_y-ϕ_y and M_z-ϕ_z) as well as section moment-curvature diagrams with respect to the neutral axis (i.e. M - ϕ) are illustrated, where $M = \sqrt{M_y^2 + M_z^2}$, and $\phi = \sqrt{\phi_y^2 + \phi_z^2}$.

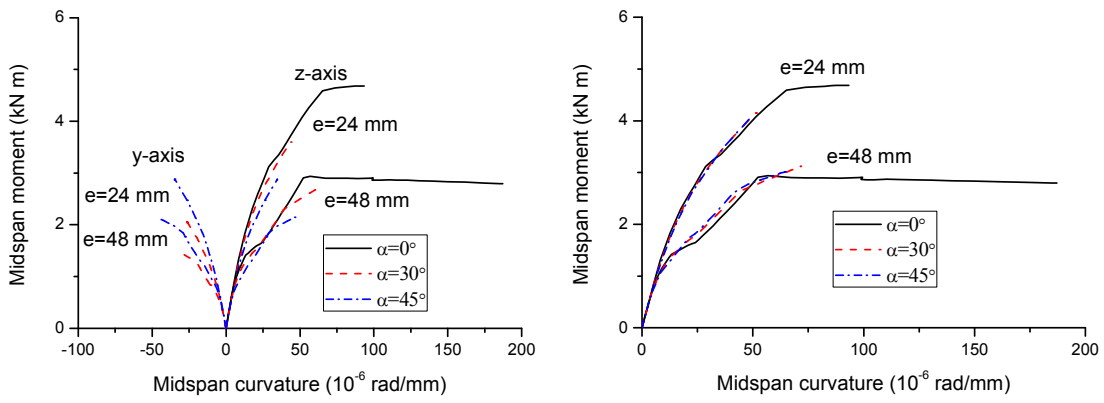

(a) Moment-curvature about y and z-axes (b) Moment-curvature about neutral axis

Fig. 5 Moment-curvature behavior

It is seen that for the columns under uniaxial eccentric loading (α = 0°), the moment-curvature curve consists of three distinct stages with two turning points corresponding to concrete cracking and steel yielding. When the tensile steel yields, the moment reaches a plateau, which is much longer for e = 48 mm than for e = 24 mm. For the columns under biaxial eccentric loading (α = 30° and 45°), on the other hand, there is no distinct yielding plateau because either the tensile steel does not yield or only one steel bar has yielded at failure as stated previously. From Fig. 5(b), it is seen that, at a given curvature level, the values of section moment for different eccentricity angles appear to be rather close. For e = 24 mm, the moment capacity developed by uniaxial eccentric loads is much higher than that by biaxial eccentric loads. This is attributed to the fact that at failure, all the reinforcing steels in the columns under biaxial eccentric loading are still in their elastic range and develop stress levels far below their yield strength. On the other hand, for e = 48 mm,

uniaxial eccentric loading leads to a little lower moment capacity than biaxial eccentric loading, partly attributed to heavier P-delta effects. It is also seen that a larger load eccentricity causes a much lower ultimate moment capacity and a significantly higher ultimate curvature.

5.2 Load-deflection behavior

Fig. 6 shows the load versus midspan lateral deflection curves for the HSC columns with different load eccentricities and eccentricity angles. The development of biaxial deflections (Δ_y and Δ_z) is demonstrated in Fig. 6(a) while total lateral deflection ($\Delta = \sqrt{\Delta_y^2 + \Delta_z^2}$) in Fig. 6(b). It is seen that a column under uniaxial eccentric loading exhibits structural softening behavior (i.e., the load decreases with increasing deflection) after yielding of tensile steel. This softening characteristic is particularly notable for a higher load eccentricity of 48 mm. However, for a column under biaxial eccentric loading, yielding of tensile steel does not result in structural softening. This can be explained by the fact that, unlike the column under uniaxial loading where all the tensile steels yield simultaneously, on yielding of the tensile steel (Bar s2) in a biaxially loaded column, all the other reinforcing steels are still in the elastic range and contribute significantly to the structural stiffness. In addition, due to smaller deflection at yielding, the P-delta effect for a column under biaxial loading is less pronounced than that for a column under uniaxial loading. It is also seen that the eccentricity angle appears to have no noticeable influence on the maximum load attained and that a higher eccentricity leads to a much lower ultimate load but a significantly higher ultimate deflection.

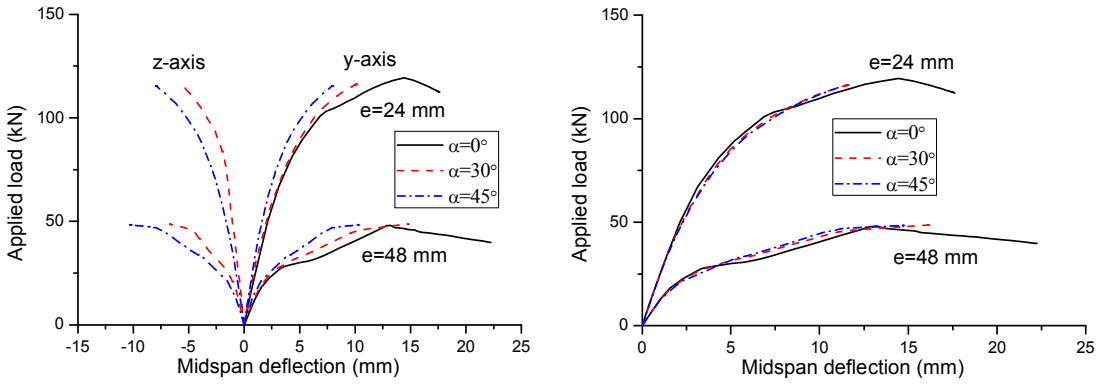

(a) Development of biaxial deflection (b) Development of total lateral deflection

Fig. 6 Load-deflection behavior

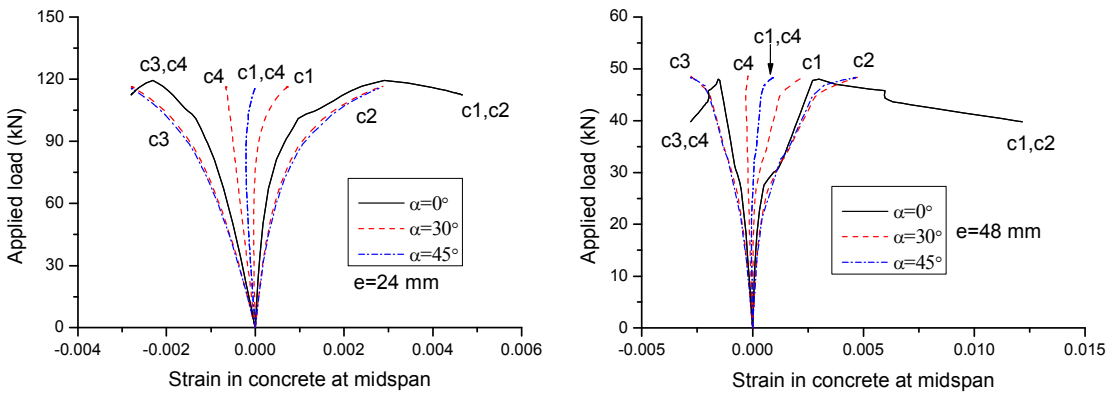

Fig. 7 Development of concrete strains

5.3 Development of concrete strains

The development of concrete strains in typical concrete fibers (c1, c2, c3 and c4) at midspan for the HSC columns with different load eccentricities and eccentricity angles is shown in Fig. 7. For the columns under uniaxial eccentric loading, c1 and c2 are the extreme tensile fibers while c3 and c4 are the extreme compressive fibers. For the columns under biaxial eccentric loading, c2 and c3 are the extreme tensile and compressive fibers, respectively. Failure of all the analyzed columns takes places when concrete in the extreme compressive fiber reaches its ultimate compressive strain, which is 0.0028 for HSC with a compressive strength of 86.2 MPa according to Eurocode 2 (CEN 2004). At failure, uniaxial eccentric loading mobilizes significantly higher concrete strain in the extreme tensile fiber than biaxial eccentric loading; and the higher the load eccentricity, the larger the value of the tensile strain in the extreme concrete fiber. This observation indicates that uniaxial eccentric loading or a higher load eccentricity leads to a larger cracking width at failure compared to biaxial eccentric loading or a lower load eccentricity.

5.4 Development of reinforcing steel stresses

Fig. 8 displays the evolution of stresses in steel bars (s1, s2, s3 and s4) at midspan for the HSC columns with different load eccentricities and eccentricity angles. For uniaxial loading, the stress in tensile steel (Bars s1 and s2) increases very slowly with increasing load up to cracking. After

that, the tensile steel stress develops rapidly and soon reaches its yield strength of 387 MPa. Meanwhile, the stress in compressive steel (Bars s3 and s4) develops in nearly a linear manner with the applied load. After yielding of tensile steel (structural softening stage), the stress in compressive steel for e = 240 mm continues to increase but, for e = 480 mm, it turns to quickly decrease.

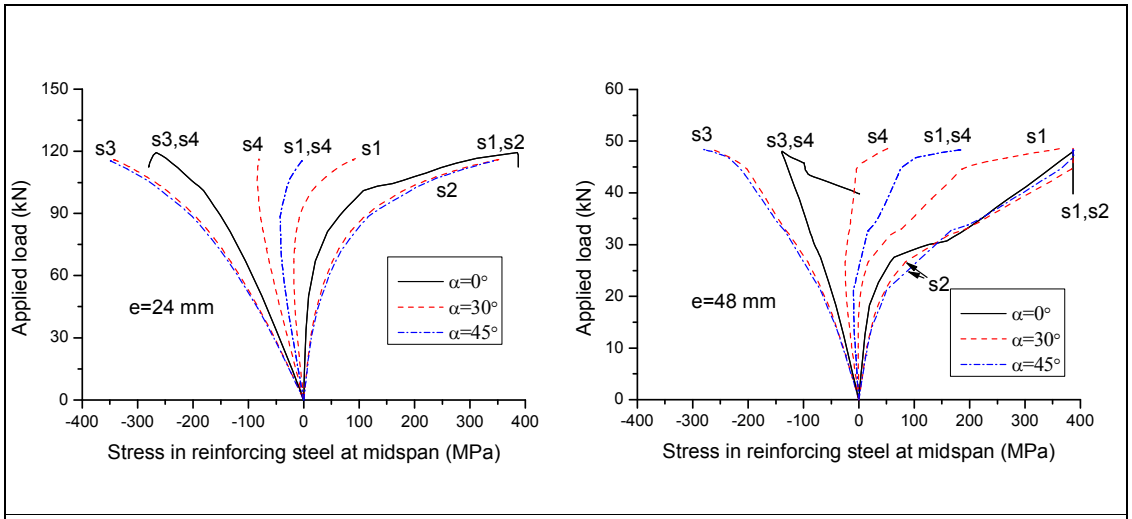

Fig. 8 Development of steel stresses

For biaxial loading, Bar s2 is subjected to tension while Bar s3 is under compression throughout the loading process. Bars s1 and s4 are under compression at first but may transit towards tension during loading, depending on the location of the neutral axis. For e = 240 mm, all the steel bars in the columns under biaxial loading have never yielded. For e = 480 mm, the tensile steel bar s2 has yielded under biaxial loading; the steel bar s4 in the column with an eccentricity angle of 30° reaches a tensile stress very close to its yield strength at failure.

5.5 Variation of neutral axis depth

Fig. 9 shows the variation of neutral axis depth at midspan with the applied load for the HSC columns with different load eccentricities and eccentricity angles. The neutral axis depth c is calculated from:

$$c = \frac{\varepsilon_{cc}}{\phi} = \frac{\varepsilon_{cc}}{\sqrt{\phi_y^2 + \phi_z^2}} \tag{25}$$

where ε_{cc} is the concrete strain at the extreme compressive fiber and ϕ is the section curvature.

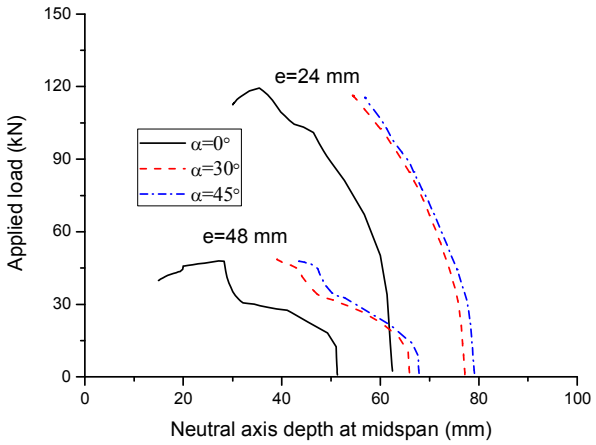

Fig. 9 Variation of neutral axis depth

It is commonly known that in a reinforced concrete member under pure bending, the neutral axis initially locates at the centroidal axis of the transformed section and remains unchanged before cracking (Lou *et al*. 2014, 2015c). For a reinforced concrete column under eccentric compression, however, the location of the initial neutral axis is dependent on both the eccentricity and eccentricity angle of the applied loads, as can be observed in Fig. 9. The shift of neutral axis during loading is influenced by some typical phases such as cracking and yielding. The decrease in neutral axis depth is slight in the elastic range but becomes crucial after concrete cracking and steel yielding (if any). At the ultimate limit state, uniaxial eccentric loading mobilizes significantly lower neutral axis depth than biaxial eccentric loading. For biaxial eccentric loading, the neutral axis depth by an eccentricity angle of 45° is a bit higher than that by an eccentricity angle of 30°. In addition, a smaller value of e results in a much higher value of c.

6. Conclusions

A nonlinear FE method for reinforced HSC slender columns subjected to biaxial eccentric loading has been developed by applying spatial Euler-Bernoulli theory. The material nonlinearity is taken into consideration by introducing the nonlinear constitutive laws of materials and by integrating the discretized concrete and reinforcing steel fibers. The geometric nonlinearity or P-delta effect is taken into account by introducing the interaction between axial and bending fields in the FE formulation. The derived stiffness matrix is composed of three components, i.e., the small displacement stiffness matrix which represents the material nonlinearity, the coupling

stiffness matrix which represents the coupling between geometric and material nonlinearities and the geometric stiffness matrix representing the large displacement (P-delta) effects. The proposed model is able to predict the inelastic response of slender HSC columns throughout all ranges of loading until failure.

The accuracy of the proposed nonlinear analysis is validated through comparisons between numerical predictions and experimental results for slender HSC test columns available in the literature. A numerical investigation is carried out by using the proposed model to illustrate the inelastic behavior of biaxially loaded slender HSC square columns, focusing on the effect of load eccentricity and eccentricity angle. Results of some important aspects of behavior are presented, including the moment-curvature and load-deflection responses, the development of concrete strains and steel stresses, and the variation of neutral axis depth. The results demonstrate that both the load eccentricity and eccentricity angle influence remarkably the structural performance of reinforced HSC slender columns.

Acknowledgments

The work has been supported by the Fundamental Research Funds for the Central Universities under Grant No. 2018IVA006.

References

Bai, Z.Z. and Au, F.T.K. (2013), "Flexural ductility design of high-strength concrete columns", *Structural Design of Tall and Special Buildings*, **22**, 92-115.

Bouchaboub, M. and Samai, M.L. (2013), "Nonlinear analysis of slender high-strength R/C columns under combined biaxial bending and axial compression", *Engineering Structures*, **48**, 37-42.

Bouzid, H and Kassoul, A. (2016), "Curvature ductility of high strength concrete beams according to Eurocode 2", *Structural Engineering and Mechanics*, **58**(1), 1-19.

Bouzid, H. and Kassoul, A. (2018), "Curvature ductility prediction of high strength concrete beams", *Structural Engineering and Mechanics*, **66**(2), 195-201.

Campione, G., Fossetti, M., Minafò, G. and Papia, M. (2012), "Influence of steel reinforcements on the behavior of compressed high strength R.C. circular columns", *Engineering Structures*, **34**, 371-382.

CEN (2004), *Eurocode 2: Design of concrete structures – Part 1-1: General rules and rules for buildings*, EN 1992-1-1, European Committee for Standardization, Brussels, Belgium.

Claeson, C. and Gylltoft, K. (1998), "Slender high-strength concrete columns subjected to eccentric loading", *ASCE Journal of Structural Engineering*, **124**(3), 233-240.

Diniz, S.M.C. and Frangopol, D.M. (1997), "Strength and ductility simulation of high-strength concrete

columns", *ASCE Journal of Structural Engineering*, **123**(10), 1365-1374.

Diniz, S.M.C. and Frangopol, D.M. (1998), "Reliability assessment of high-strength concrete columns", *ASCE Journal of Engineering Mechanics*, **124**(5), 529-536.

Diniz, S.M.C. and Frangopol, D.M. (2003), "Safety evaluation of slender high-strength concrete columns under sustained loads", *Computers and Structures*, **81**(14), 1475-1486.

Ho, J.C.M., Lam, J.Y.K. and Kwan, A.K.H. (2010), "Effectiveness of adding confinement for ductility improvement of high-strength concrete columns", *Engineering Structures*, **32**, 714-725.

Hung, C.C. and Hu, F.Y. (2018), "Behavior of high-strength concrete slender columns strengthened with steel fibers under concentric axial loading", *Construction and Building Materials*, **175**, 422-433.

Jumaa, G.B. and Yousif, A.R. (2019), "Size effect in shear failure of high strength concrete beams without stirrup reinforced with basalt FRP bars", *KSCE Journal of Civil Engineering*, **23**(4), 1636-1650.

Kim, J.K. and Yang, J.K. (1995), "Buckling behaviour of slender high-strength concrete columns", *Engineering Structures*, **17**(1), 39-51.

Lee, H.J. (2013), "Predictions of curvature ductility factor of doubly reinforced concrete beams with high strength materials", *Computers and Concrete*, **12**(6), 831-850.

Lou, T., Liu, M., Lopes, S.M.R. and Lopes, A.V. (2017), "Moment redistribution in two-span prestressed NSC and HSC beams", *Materials and Structures*, **50**, 246.

Lou, T., Lopes, S.M.R. and Lopes, A.V. (2014), "FE modeling of inelastic behavior of reinforced high-strength concrete continuous beams", *Structural Engineering and Mechanics*, **49**(3), 373-393.

Lou, T., Lopes, S.M.R. and Lopes, A.V. (2015a), "FE analysis of short- and long-term behavior of simply supported slender prestressed concrete columns under eccentric end axial loads causing uniaxial bending", *Engineering Structures*, **85**, 52-62.

Lou, T., Lopes, S.M.R. and Lopes, A.V. (2015b), "Redistribution of moments in reinforced high-strength concrete beams with and without confinement", *Structural Engineering and Mechanics*, **55**(2), 379-398.

Lou, T., Lopes, S.M.R. and Lopes, A.V. (2015c), "Neutral axis depth and moment redistribution in FRP and steel reinforced concrete continuous beams", *Composites Part B: Engineering*, **70**, 44-52.

Ma, C., Awang, A.Z. and Omar, W. (2016), "Flexural ductility design of confined high-strength concrete columns: Theoretical modeling", *Measurement*, **78**, 42-48.

Pallarés, L., Bonet, J.L., Miguel, P.F. and Fernández-Prada, M.A. (2009), "The influence of the weak axis on the behavior of high strength RC slender columns subjected to biaxial bending", *Engineering Structures*, **31**, 487-497.

Pallarés, L., Bonet, J.L., Miguel, P.F. and Fernández-Prada, M.A. (2008), "Experimental research on high strength concrete slender columns subjected to compression and biaxial bending forces", *Engineering Structures*, **30**, 1879-1894.

Saatcioglu, M. and Razvi, S.R. (1998), "High-strength concrete columns with square sections under concentric compression", *ASCE Journal of Structural Engineering*, **124**(12), 1438-1447.

Teixeira, M.M. and Bernardo, L.F.A. (2018), "Ductility of RC beams under torsion", *Engineering Structures*,

168, 759-769.

Teng, J.G., Xiao, Q.G., Yu, T. and Lam, L. (2015), "Three-dimensional finite element analysis of reinforced concrete columns with FRP and/or steel confinement", *Engineering Structures*, **97**, 15-28.